Supporting Information

Pisliakov et al. 10.1073/pnas.0909150106

SI Text

1. Computational Methods and Computational Studies. This section provides details about the specific studies performed in this work. It also provides a further description of the renormalization approach developed here.

1.1. Simulating the Chemical Reaction of Adenylate Kinase (ADK). The overall reaction mechanism of ADK can be described by the steps depicted in Fig. S1 (see also, e.g., ref. 1), and the chemical details of this reaction are shown in Fig. S2. We will consider two possible mechanisms here. The action of the protein starts upon the binding of the substrate to the protein in its open configuration, which is then followed by a conformational motion of the protein to its closed configuration and finally by a phosphoryl transfer reaction. The open and closed configurations are depicted in Fig. S3. To model the reaction in the protein, we first need to have a clear idea about the relevant reference reaction in solution, and this issue is addressed in this section.

In principle, this reaction is a simple nucleophilic displacement reaction, in which a negatively charged oxygen atom on AMP acts as a nucleophile, attacking the P_γ of ATP, to yield a transition state in which the P_γ has pentavalent coordination. This transition state then dissociates to yield two ADP. To analyze the energetics of this reaction, we started with a systematic study of the corresponding reference reaction in solution. We evaluated the two-dimensional (2-D) free energy surface by means of careful reaction coordinate mapping. Our reaction coordinates were defined as a function of the P_γ–O_{nuc} and P_γ–O_{lg} distances, which were each mapped from 1.6 Å to 2.8 Å in 0.15-Å increments. All ab initio calculations were performed by using the Gaussian03 software package (2). For simplicity, adenosine was substituted by a methyl group throughout. The geometry at each point on the free energy surface was obtained by means of gas-phase optimizations by using the 6–31+G* basis set and the MPW1PW91 hybrid functional (3). Solvation was subsequently simulated as a single point correction to the SCF energy by using the COSMO (4, 5) continuum model. The resulting free energy surface was then used to identify the location of key stationary points, and all energies are given relative to the sum energies of the nucleophile and substrate at infinite separation. Note that more in-depth studies of the reaction mechanism by using hybrid quantum mechanical/molecular mechanical free energy perturbation approaches will be done in the future. Finally, the configurational entropy ($-T\Delta S_{conf}$) was evaluated by means of the restraint release approach, as outlined in detail in refs. 6 and 7. The approach used here has been shown to successfully reproduce experimental free energies for phosphate hydrolysis (8–12).

When examining the reaction mechanism, it is important to consider the fact that the nucleophilic AMP may be protonated at P_α, with this proton being transferred onto the γ-phosphate during the reaction, but there is no experimental data available addressing this issue. Thus, for comparison, we have considered AMP attack on ATP in solution both for the case when the AMP is not protonated and for the case when the AMP is protonated at P_α. The resulting free energy surfaces (as well as the corresponding transition state geometries) are shown in Fig. S4 *A* and *B*, respectively. An examination of the free energy surfaces for both phosphoryl transfer reactions shows that the pathway is not dependent on the protonation state—as, regardless of the protonation state of the nucleophile, the reaction proceeds through a concerted A_ND_N pathway (a detailed discussion of the different mechanistic possibilities can be found in, e.g., refs. 9, 13, and 14) with a single transition state in which bond formation to the nucleophile and bond cleavage to the leaving group occur simultaneously—and that the reaction pathway is overall associative in nature. However, the precise transition state varies according to the protonation state of the nucleophile, as shown in Fig. S4. When the nucleophile is not protonated, the reaction proceeds via a more expansive transition state, with P–O distances of 1.9 Å and 2.5 Å to the nucleophile and leaving group respectively, and a barrier of 21.4 kcal/mol. In comparison, the transition state for the reaction where the nucleophile is protonated at P_α is significantly more compact, with P–O distances of 1.9 Å and 1.75 Å to the nucleophile and leaving group, respectively. Additionally, $\Delta g^{\neq}_{calc}$ is 4.6 kcal/mol higher when the nucleophile is protonated at P_α (26.0 kcal/mol), as compared with the situation where the nucleophile is not protonated. Combining this finding with the fact that the system with the protonated AMP gives a higher barrier with the pK_a difference between the nucleophile and substrate [5.83 for ATP complexed to a magnesium cation (15), and 6.1 and 3.3 for AMP in the two different protonation states respectively (16)] strongly suggests that even though both mechanisms are possible, the most likely scenario is one in which the reaction in ADK proceeds via a deprotonated nucleophile, and this is therefore the mechanism considered in the remainder of this work.

Once we obtained a reasonable description of the solution reaction, we turned to the description of the enzymatic reaction. For this purpose, we used the empirical valence bond (EVB) method, which is a well-established and effective approach, especially in situations where extended sampling is needed (e.g., ref. 17). The EVB method has been described extensively elsewhere (18, 19), and we provide here only the most relevant points.

As a first step, we built a solution EVB surface and calibrated this surface by using the ab initio solution surface for the mechanism shown in Fig. S2*A* (in which the AMP is not protonated). The corresponding EVB free energy profile for the solution reaction, as well as the resonance structures used, are shown in Fig. S5. The calibrated EVB parameters were then used (unchanged) to generate the EVB surface of the reaction in the closed configuration of the protein (i.e., at this step, we replaced the environment of the reaction in solution by the actual protein). Here, the initial structure of the enzyme in the closed configuration (20) was taken from the Protein Data Bank (21) (PDB code: 2rgx), and the ligands were introduced via a docking procedure, followed by a long relaxation run. The EVB calculations involved a free energy perturbation umbrella sampling (FEP-US) procedure (18, 19), which was performed while using 11 windows of 100 ps each, with a 1-fs time step. The resulting EVB surface for the ADK reaction is shown in Fig. S5 along with the profile obtained in solution. The calculated barriers for the reaction in the enzyme and in solution are 20 kcal/mol and 40 kcal/mol, respectively, whereas the corresponding observed barrier in the enzyme is ≈14 kcal/mol. In the case of the solution reaction, there is no experimental estimate of this barrier in the literature, and we can therefore only assess it from calculations. It should also be noted that although we could have invested even more effort into the evaluation of the surfaces of both the solution and the protein reactions, such an investment is not directly relevant to the issue here, as our aim is not to deeply characterize ADK but rather to explore the link between conformational dynamics and chemistry.

In previous works (22), we demonstrated that the EVB approach can be used to effectively map the entire catalytic landscape of enzymatic reactions and not only the profile at the Michaelis Complex. This approach was achieved by mapping the activation free energy for the chemical step in different regions of the conformational space. The same approach was used here, where we focused on the changes in the reaction profile upon increasing the distance between the donor and acceptor. In doing so, it was assumed that the increase in this distance is correlated with the conformational motion toward the open form.

1.2 Renormalizing the Energetics of the Enzymatic Reaction. Having characterized the catalytic landscape of the full model, we subsequently moved to the reduced representations. This involved a multilevel hierarchical renormalization approach in which we first mapped the full-atom protein+solvent explicit system (model A), with the coordinate set **r**, onto a coarse-grained (CG) simplified protein model (model B), in which each side chain is represented by a sphere (23) with a coordinate set **q**, and finally on a 2-D simplified model (model C), with the coordinates Q_1 and Q_2. The aim of this step of the "renormalization" process is to force the three models to have equivalent energetics.

The 2-D surface was constructed in the space defined by the chemical process (in terms of the chemical reaction coordinate) and the conformational coordinate (defined by the motion between the open and closed configurations). It was assumed that the donor–acceptor distance is correlated with the conformational coordinate (or that the donor and acceptor are bound to the protein in the phosphoryl transfer step). Of course, the chemical coordinate includes all of the protein reorganization during the chemical step.

The actual 2-D surface was obtained from the ground-state energy, E_g, of a 2-D, four-state, EVB-type potential Hamiltonian, whose diagonal elements are given by

$$H_{lm,lm} = \varepsilon_{\mathrm{lm}} = \frac{\hbar\omega_1}{2}(Q_1 - F_{\mathrm{coupl}}\delta_1^{lm})^2 + \frac{\hbar\omega_2}{2}(Q_2 - \delta_2^{lm})^2 + \alpha_{lm}. \quad \textbf{[S1]}$$

Here Q_1 and Q_2 are the chemical and conformational coordinates, respectively, both indices l and m can have the values of 1 and 2, and the parameter α_{lm} defines the free energy in the four minima of the surface (OR, OP, CR and CP, where O, C, R, and P designate the open, closed, reactant, and product states, respectively; for example $l = 1$, $m = 1$ corresponds to the OR state). Both Q_1 and Q_2 were defined as the effective dimensionless coordinates: $Q_1 = -(\varepsilon_{21} - \varepsilon_{11})\,\hbar\omega_1\delta_1$ and $Q_2 = -(\varepsilon_{12} - \varepsilon_{11})\,\hbar\omega_2\delta_2$. The shifts, δ_i, are related to each other by $\delta_1^{21} = \delta_1^{22} = -\delta_1^{11} = \delta_1$, $\delta_1^{12} = \delta_1^{11}$, $\delta_2^{12} = \delta_2^{22} = -\delta_2^{11} = \delta_2$, $\delta_2^{22} = \delta_2^{11}$. The function, F_{coupl}, reflects the change in the chemical reorganization energy upon change in the donor–acceptor distance in the case when this distance is coupled to the conformational coordinate Q_2. (F_{coupl} is defined as follows: $F_{\mathrm{coupl}} = 1+(G\mathrm{x}Q_2) / \delta_2$ (where G is a constant) for $Q_2 > \delta_2$ and $F_{\mathrm{coupl}} = 1$ for $Q_2 < \delta_2$). The effective frequency is evaluated by $\omega_{\mathrm{eff}} = \int \omega P(\omega) d\omega$, where $P(\omega)$, is the normalized power spectrum of the corresponding contribution to $(\varepsilon_{2m} - \varepsilon_{1m})$. The δ terms are related to the corresponding reorganization energies by:

$$\lambda_1 = (\hbar/2)\omega_1\delta_1^2,\ \lambda_2 = (\hbar/2)\omega_2\delta_2^2. \quad \textbf{[S2]}$$

In addition to the diagonal Hamiltonian elements, i.e., minima energies ε_i, we also have off-diagonal elements, whose values are chosen to force the barriers along each coordinate to agree with estimates of the corresponding experimental barriers. The actual potential surface, E_g, is then obtained by diagonalizing the system Hamiltonian defined by Eq. **S1**.

Finally, to control the dynamical behavior of the surface along the conformational coordinate, we (in some cases) introduced an additional contribution to ε_{lm} which modulates the surface in the Q_2 direction, namely a combination of several periodic functions with adjustable amplitudes and frequencies:

$$F_{fast} = a_1\cos(b_1Q_2) + a_2\cos(b_2Q_2) + a_3\cos(b_3Q_2). \quad \textbf{[S3]}$$

This adds more flexibility in adjusting the autocorrelation of the conformational motion and also makes the landscape along the conformational coordinate more "corrugated", thus allowing one to capture the multiminima effect of the corresponding protein surface.

1.3 Renormalizing the Dynamics of the Enzymatic Reaction. Our next challenge is to simulate the dynamics in the space defined by the effective coordinates in a way that represents the long timescale behavior of the real system. This challenge is addressed by adopting the same type of three-step hierarchical renormalization model as described above, but by now focusing on forcing the three models to have equivalent dynamics. The first step in this process is achieved by reaching a correspondence between the dynamics of models A and B. This is done by first generating two different sets ($\mathbf{r}_1$ and $\mathbf{r}_2$) of coordinates in the full model, and subsequently generating the corresponding two sets ($\mathbf{q}_1$ and $\mathbf{q}_2$)in the CG model. Regular MD simulations are then used in the model A to evaluate the time (τ_{trans}) of moving from $\mathbf{r}_1$ to $\mathbf{r}_2$ under the influence of a constraint potential,

$$U_{\mathrm{con}} = K_{\mathrm{con}}(|\mathbf{r} - \mathbf{r}_2|)^2 \quad \textbf{[S4]}$$

where K_{con} is a force constant (the large value of K_{con} is needed to obtain this transition in a reasonable time).

The procedure is then repeated in the model B for moving from $\mathbf{q}_1$ to $\mathbf{q}_2$ under a constraint U_{con}' (with the same values of K_{con}). The dynamics of the CG model is simulated by Langevin Dynamics (LD) (24, 25);

$$m_k\ddot{q}_k' = -m_k\gamma_q\dot{q}_k' - \frac{\partial E_s}{\partial q_k'} - \frac{\partial U_{\mathrm{con}}'}{\partial q_k'} + A_k'(t) \quad \textbf{[S5]}$$

where k runs over the components of the vector **q**, γ_q and m_k are the friction and mass of the q_k' coordinate (the prime in this term designates dimensionless coordinates), $A_k'(t)$ is a random force that satisfies the fluctuation–dissipation relationship, E_s is the potential of the simplified protein model, and U'_{con} is the restraint potential that corresponds to Eq. **S4** (with the same K_{con} but with coordinates **q** instead of **r**). The friction constant, γ_q, is adjusted so that the time of moving from $\mathbf{q}_1$ to $\mathbf{q}_2$ becomes similar to that of moving from $\mathbf{r}_1$ to $\mathbf{r}_2$ for the chosen value of K_{con}. The best friction constant is obtained by using the smallest value of K_{con} that moves from $\mathbf{r}_1$ to $\mathbf{r}_2$ within reasonable simulation times. Note that the use of a strong constraint allows us to explore some aspects of the friction experienced by the system during large structural changes, which cannot be explored otherwise.

The next task is to reach a correspondence between the dynamics of the CG simplified model and the 2-D model. To do so, we start by evaluating the dynamics of the two effective coordinates on the 2-D surface by a LD treatment which follows the formulation of (24), i.e.

$$M_\alpha\ddot{Q}_\alpha' = -M_\alpha\Gamma_\alpha\dot{Q}_\alpha' - \frac{\partial E}{\partial Q_\alpha'} - \frac{\partial U_{\mathrm{con}}''}{\partial Q_\alpha'} + A_\alpha'(t) \quad \textbf{[S6]}$$

where $\alpha = 1, 2$ corresponds to the effective conformational and chemical coordinates, respectively, $Q_\alpha = (M_\alpha\omega_\alpha/\hbar)^{1/2}\, Q'_\alpha$, $\delta_\alpha = (M_\alpha\omega_\alpha/\hbar)^{1/2}\, \delta'_\alpha$, $M_\alpha = k_BT/\langle(\dot{Q}'_\alpha)^2\rangle$ and Γ_α are the effective mass and friction of these two coordinates, k_B is Boltzmann's constant, T is the temperature, and $U_{\rm con}''$ is a constraint potential in the model C. The key issue here is to force the dynamics of the simplified 2-D model to correspond to that of the full atomistic model. Because the CG model has already been fitted to the full model, we can fit the 2-D model to the CG model (i.e., model C to model B). As in the "fitting" of the dynamics of models A and B, we again evaluate the transition time for moving between the two generated sets of coordinates in each model (e.g., the time required to move between two significantly different coordinate sets $\mathbf{q}_1'$ and $\mathbf{q}_2'$ in model B should correspond to the time of moving between the equivalent coordinates in model C) for different values of the applied constraint. We then refine the friction, Γ_α, by comparing the transition time obtained from the dynamics in different models.

The next important element (the "fine-tuning" of the dynamical properties at different timescales) of our renormalization approach is the requirement that the autocorrelation of the energy gap and other related properties will have similar behavior in all three models used in this study. The details of this part are given in the next section for the specific example of ADK.

1.4. Forcing the Dynamics of ADK to Be Similar in the Different Models. As stated above, our renormalization procedure is aimed at capturing the dynamics of the full model in both the CG and 2-D models. This strategy was applied in the present work to the modeling of ADK, starting by applying a strong constraint to all three models, driving each system from the open to the closed structure, and then adjusting the friction constants γ_q (in model B) and Γ_α (in model C) to get similar time dependence to that obtained in the full model. The corresponding process is described in Fig. S6. In principle, we could obtain a more accurate representation of the full model by the reduced models if we use the above approach on a longer timescale (while using a weaker constraint), but this is out of the scope of the present work.

We further refined the dynamical properties for the short timescale range of the simplified models by calculating the short timescale autocorrelation functions (ACF) of the conformational coordinates for several different friction constants and subsequently selected the friction constants that gave the best agreement with the ACF of the full model (see Fig. S7). The use of different values of γ_q in Fig. S7 demonstrates part of our fitting procedure. Finally, we also forced the short-time dynamics of the chemical coordinate of the three models to be similar by requiring that the autocorrelations of the energy gap are similar. The resulting short timescale dynamics of the chemical coordinate of the three models is given in Fig. S8. Overall, even though the fitting is not perfect (e.g., better agreement could be obtained by having two different friction constants in the CG model: one for the chemical and one for the conformational changes), it is adequate for the purposes of this work. Moreover, in principle we might invoke time-dependent friction kernels (26, 27). However, such treatments are not justified at the present stage because the friction constants used already provide a reasonable starting point for the analysis reported in the text. Furthermore, we have examined dynamical effects for drastically different effective frictions by changing the "corrugation" of the system (and the relevant corresponding correlation time), by the use of Eq. **S3** (see also Fig. 3 of the main text).

Armed with a reasonably calibrated model, we can then explore the long timescale motions by using the 2-D model (without any constraints). The results of such simulations are shown in Fig. 2 of the main text. The simulated results can be qualitatively converted to motions in the CG model, as shown in the Movie S1. However, here we focus mainly on using the 2-D model to explore the dynamical proposal, as is discussed in the main text and *Exploring Dynamical Effects*.

2. Exploring Dynamical Effects. Defining the issues in the field can benefit from considering the diagram in Fig. S9. As seen from the figure, we can represent the key hypothesis in one of two ways. The first of these is a diffusive model (Fig. S9 *A* and *B*). In this model, the energy of the conformational motion is completely dissipated before the chemical process. The alternative is an inertial model (Fig. S9 *C* and *D*), where the conformational motion is somehow "remembered" during the chemical motion, and thus this represents a true and well-defined dynamical effect, which can presumably enhance the chemical rate. The work summarized in the main text (and particularly in Figs. 3 and 4) demonstrates that the motions on the conformational–chemical landscape are extremely unlikely to correspond to the inertial model, at least as long as the chemical barrier is higher than a few k_BT. In general, as shown in Fig. 3, the inertial model is also unlikely to be valid as long as the barriers between the different configurations in the ground state are lower than the chemical barrier. In this case the solution of the multistate rate equation for the system will follow the trend dictated by the highest activation barriers. It is also useful to note that, in practice, the chemical barriers in most enzymes are greater than the diffusion limit ($\approx$9 kcal/mol) and are thus likely to be the determining factor for the overall rate, an issue that has been discussed at length in recent studies of both choristmate mutase (28) and DNA polymerase (29). It is true, of course, that neither of these works addressed the hypothetical scenario in which the barrier for the binding step is much higher than the chemical barrier, but this is anyhow a highly unlikely scenario. That is, there is no evolutionary pressure to reduce the chemical barrier for an enzyme-catalyzed reaction far below the diffusion controlled limit, making it improbable that the chemical barrier will be much lower than the binding (or product release) barrier. However, such a hypothetical case was in fact modeled recently (30).

The present work has also examined the related intriguing proposal that the binding energy of the substrate can be used to induce the conformational change, with the resulting kinetic energy driving the chemical reaction and this study is described in Figs. 4 and 5 of the main text. Overall, we established that the kinetic energy of the conformational motion is dissipated before the chemical step, for cases with a significant chemical barrier. However, for the case with a very low chemical barrier, we found that trajectories that start from a slightly open structure and move with excess kinetic energy to the closed form take a longer amount of time to cross the chemical barrier than trajectories that start from the closed form. For example, when using strong constraints of 5 kcal mol^{-1}Å^{-2}, we found that the first passage times are $\approx$100 ps and $\approx$280 ps for trajectories that start at the closed and partially open structures respectively. This effect reflects excursions in the conformational space, which can slow down the arrival of the trajectory to the optimal point for crossing the chemical barrier.

1. Wolf-Watz M, et al. (2004) Linkage between dynamics and catalysis in a thermophilic-mesophilic enzyme pair. *Nat Struct Mol Biol* 11:945–949.
2. Frisch MJ, et al. (2004) *GAUSSIAN 03* (*Revision C*. 02).
3. Adamo C, Barone V (1998) Exchange functionals with improved long-range behavior and adiabatic connection methods without adjustable parameters: The mPW and mPW1PW models. *J Chem Phys* 108:664–675.
4. Barone V, Cossi M (1998) Quantum calculation of molecular energies and energy gradients in solution by a conductor solvent model. *J Phys Chem A* 102:1995–2001.
5. Klamt A, Schüürmann GJ (1993) COSMO: A new approach to dielectric screening in solvents with explicit expressions for the screening energy and its gradient. *J Chem Soc Perkin Trans 2* 5:799–805.

6. Strajbl M, Sham YY, Villa J, Chu ZT, Warshel A (2000) Calculation of activation entropies of chemical reactions in solution. *J Phys Chem B* 104:4578–4584.
7. Sharma PK, Xiang Y, Kato M, Warshel A (2005) What are the roles of substrate assisted catalysis and proximity effects in peptide bond formation by the ribosome? *Biochemistry* 44:11307–11314.
8. Klahn M, Rosta E, Warshel A (2006) On the mechanism of hydrolysis of phosphate monoester dianions in solution and proteins. *J Am Chem Soc* 128:15310–15323.
9. Rosta E, Kamerlin SCL, Warshel A (2008) On the interpretation of the observed LFER in phosphate hydrolysis: A thorough computational study of phosphate diester hydrolysis in solution. *Biochemistry* 47:3725–3735.
10. Kamerlin SCL, Florian J, Warshel A (2008) Associative versus dissociative mechanisms of phosphate monoester hydrolysis: On the interpretation of activation entropies. *Chem Phys Chem* 9:1767–1773.
11. Kamerlin SCL, Williams NH, Warshel A (2008) Dineopentyl phosphate hydrolysis: Evidence for stepwise water attack. *J Org Chem* 73:6960–6969.
12. Kamerlin SCL, Haranczyk M, Warshel A (2009) Are mixed explicit/implicit solvation models reliable for studying phosphate hydrolysis? A comparative study of continuum, explicit and mixed solvation models. *Chem Phys Chem* 10:1125–1134.
13. Wilkie J, Gani D (1996) Comparison of inline and non-inline associative and dissociative reaction pathways for model reactions of phosphate monoester hydrolysis. *J Chem Soc Perkin Trans 2* 2:783–787.
14. Kamerlin SCL, Wilkie J (2007) The role of metal ions in phosphate ester hydrolysis. *Org Biomol Chem* 5:2098–2108.
15. Shikama K (1971) Standard free energy maps for the hydrolysis of ATP as a function of pH, pMg and pCa. *Arch Biochem Biophys* 147:311–317.
16. Westheimer FH, Jencks WP (2003) *Aqueous pK_a Values*. (Am Chem Soc, Washington DC).
17. Roca M, Vardi-Kilshtain A, Warshel A (2009) Toward accurate screening in computer-aided enzyme design. *Biochemistry* 48:3046–3056.
18. Warshel A (1991) *Computer Modeling of Chemical Reactions in Enzymes and Solutions* (John Wiley & Sons, New York).
19. Åqvist J, Warshel A (1993) Simulations of enzyme reactions using valence bond force fields and other hybrid quantum/classical approaches. *Chem Rev* 93:2523–2544.
20. Henzler-Wildman KA, et al. (2007) Intrinsic motions along an enzymatic reaction trajectory. (PDB ID: 2rgx). *Nature* 450:838–844.
21. Berman HM, et al. (2000) The protein data bank. *Nucl Acids Res* 28:235–242.
22. Roca M, Messer B, Hilvert D, Warshel A (2008) On the relationship between folding and chemical landscapes in enzyme catalysis. *Proc Natl Acad Sci USA* 105:13877–13882.
23. Levitt M, Warshel A (1975) Computer simulation of protein folding. *Nature* 253:694–698.
24. Braun-Sand S, Strajbl M, Warshel A (2004) Studies of proton translocations in biological systems: Simulating proton transport in carbonic anhydrase by EVB based models. *Biophys J* 87:2221–2239.
25. McQuarrie DA (1976) *Statistical Mechanics* (Harper and Row, New York).
26. Adelman SA (1976) Fokker-plank equations for simple non-Markovian systems. *J Chem Phys* 64:124–130.
27. Grote RF, Hynes JT (1980) The stable states picture of chemical reactions. II. Rate constants for condensed and gas phase reaction models. *J Chem Phys* 73:2715–2732.
28. Roca M, Messer B, Hilvert D, Warshel A (2008) On the relationship between folding and chemical landscapes in enzyme catalysis. *Proc Natl Acad Sci USA* 105:13877–13882.
29. Xiang Y, Goodman MF, Beard WA, Wilson SH, Warshel A (2008) Exploring the role of large conformational changes in the fidelity of DNA polymerase β. *Proteins* 70:231–247.
30. Min W, Xie XS, Baghchi B (2008) Two-dimensional reaction free energy surfaces of catalytic reaction: Effects of protein conformational dynamics on enzyme catalysis. *J Phys Chem B* 112:454–466.

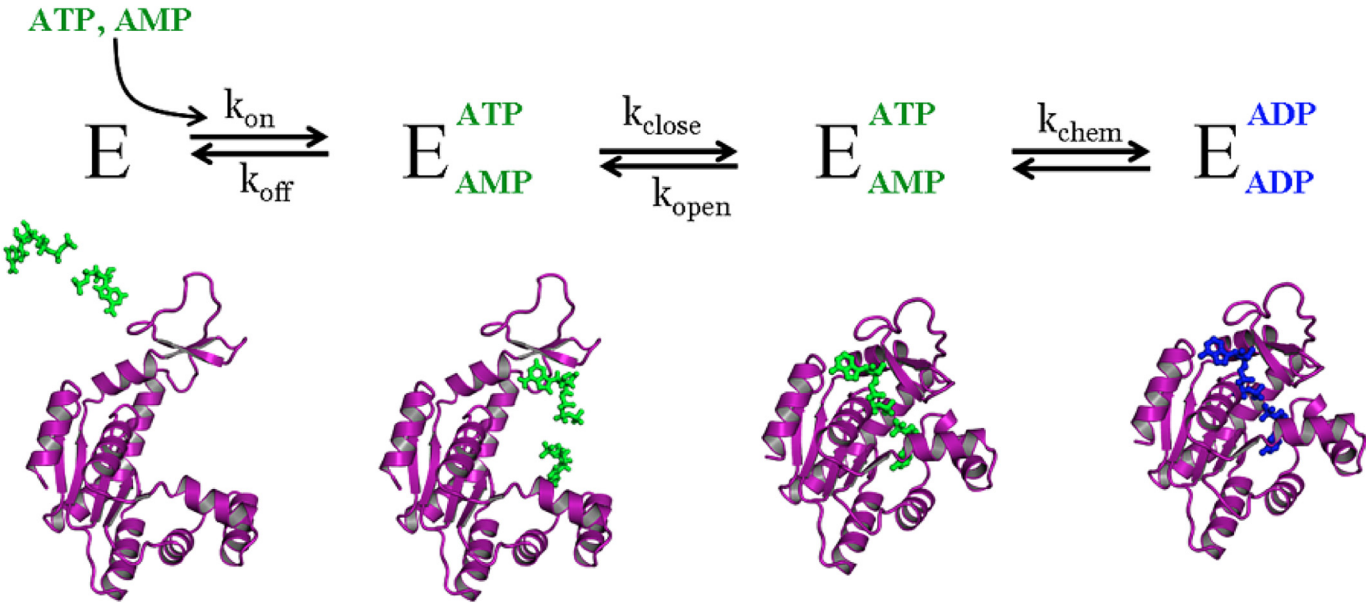

Fig. S1. The ADK reaction scheme, with rates corresponding to the different steps in the reaction. Namely, substrate binding and dissociation (k_{on}/k_{off}), the conformational change (k_{close}/k_{open}), and the chemical step (k_{chem}).

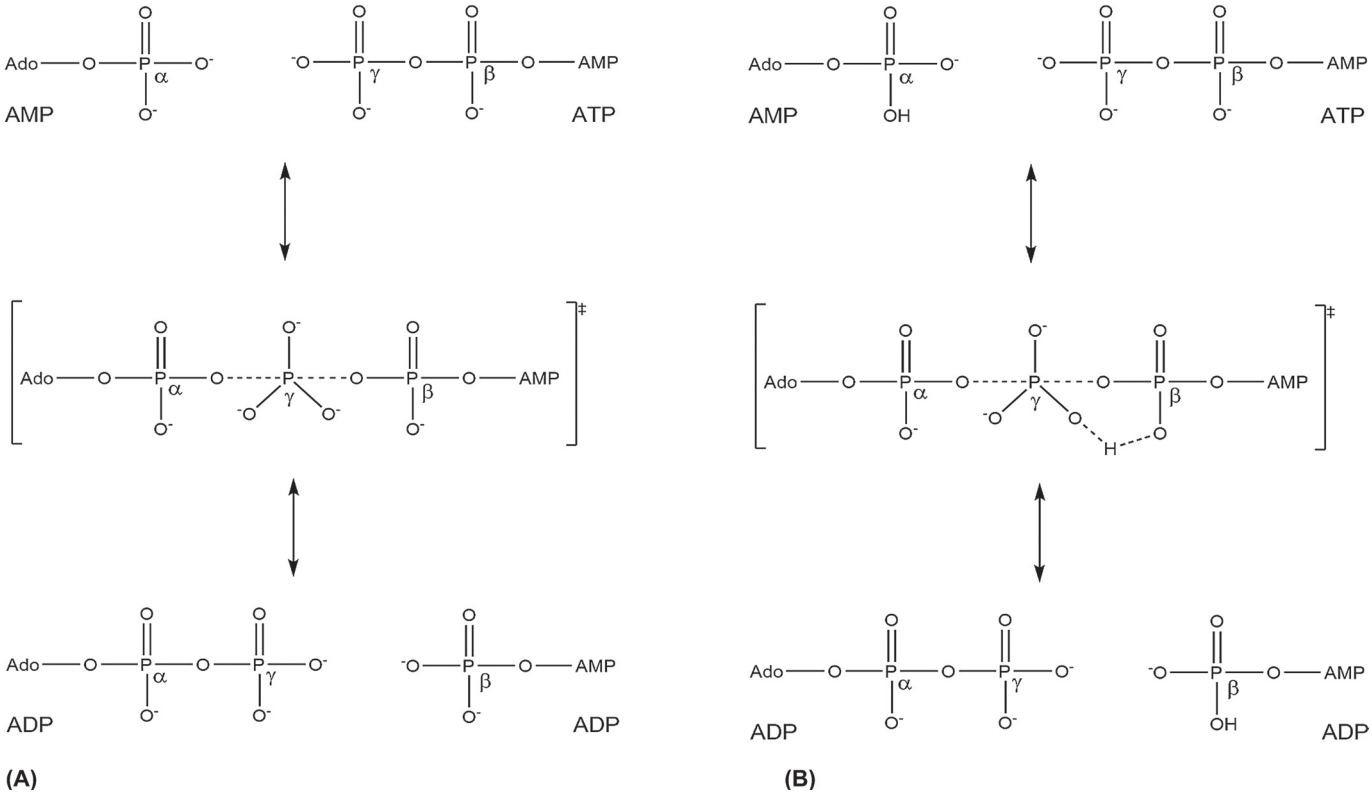

Fig. S2. The two possible pathways in the reaction mechanism of adenylate kinase, in which the AMP is not protonated (*A*), and the AMP is protonated at P_α (*B*).

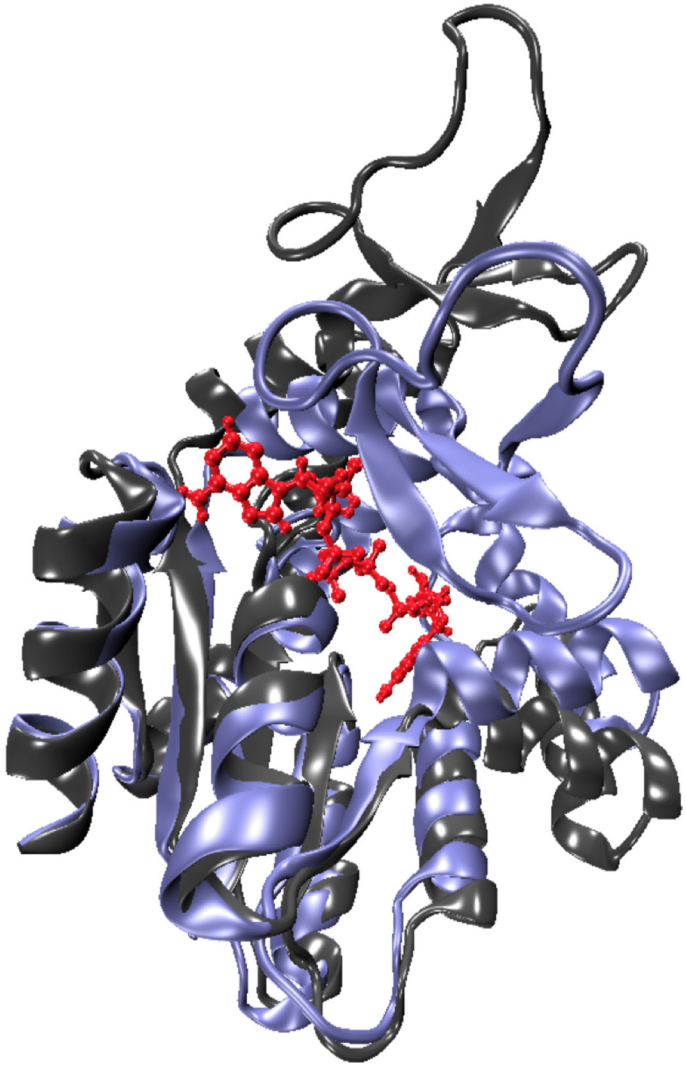

Fig. S3. The structures of the open (dark gray) and closed (ice blue) forms of ADK.

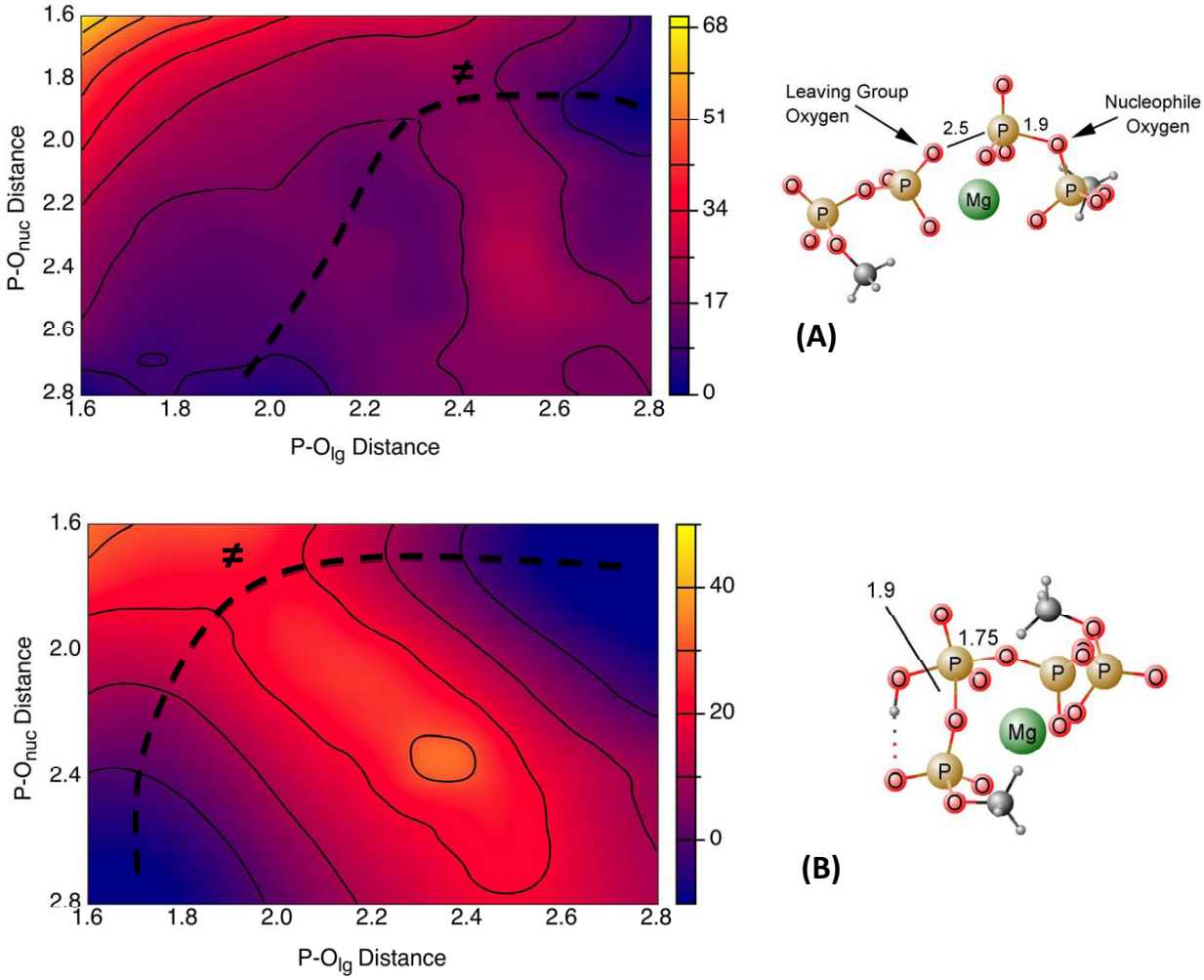

Fig. S4. The calculated free energy surfaces and corresponding transition states for the reference solution reaction when the AMP is unprotonated (*A*) and protonated at P_α (*B*).

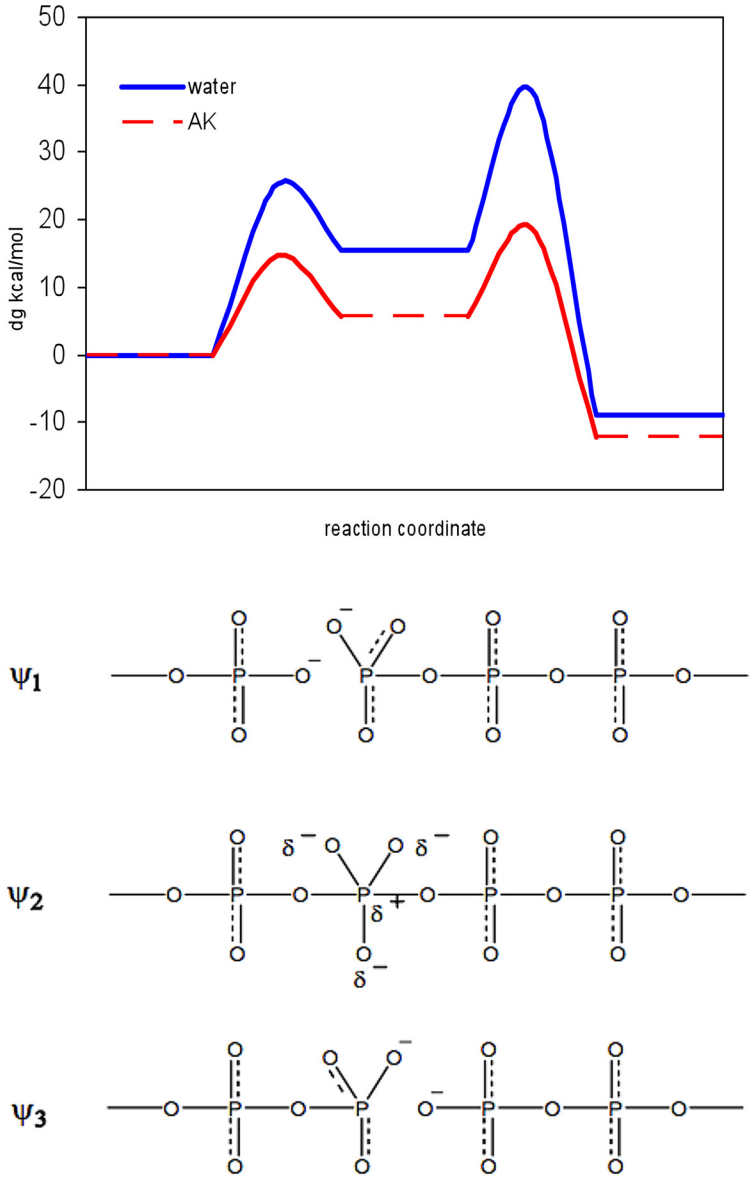

Fig. S5. The EVB free energy surface for the reaction in the protein and in the solution as well as the resonance structures used for modeling this reaction. The EVB calculations involved the FEP-US procedure, which was performed in 11 windows of 100 ps each, using a 1-fs time step.

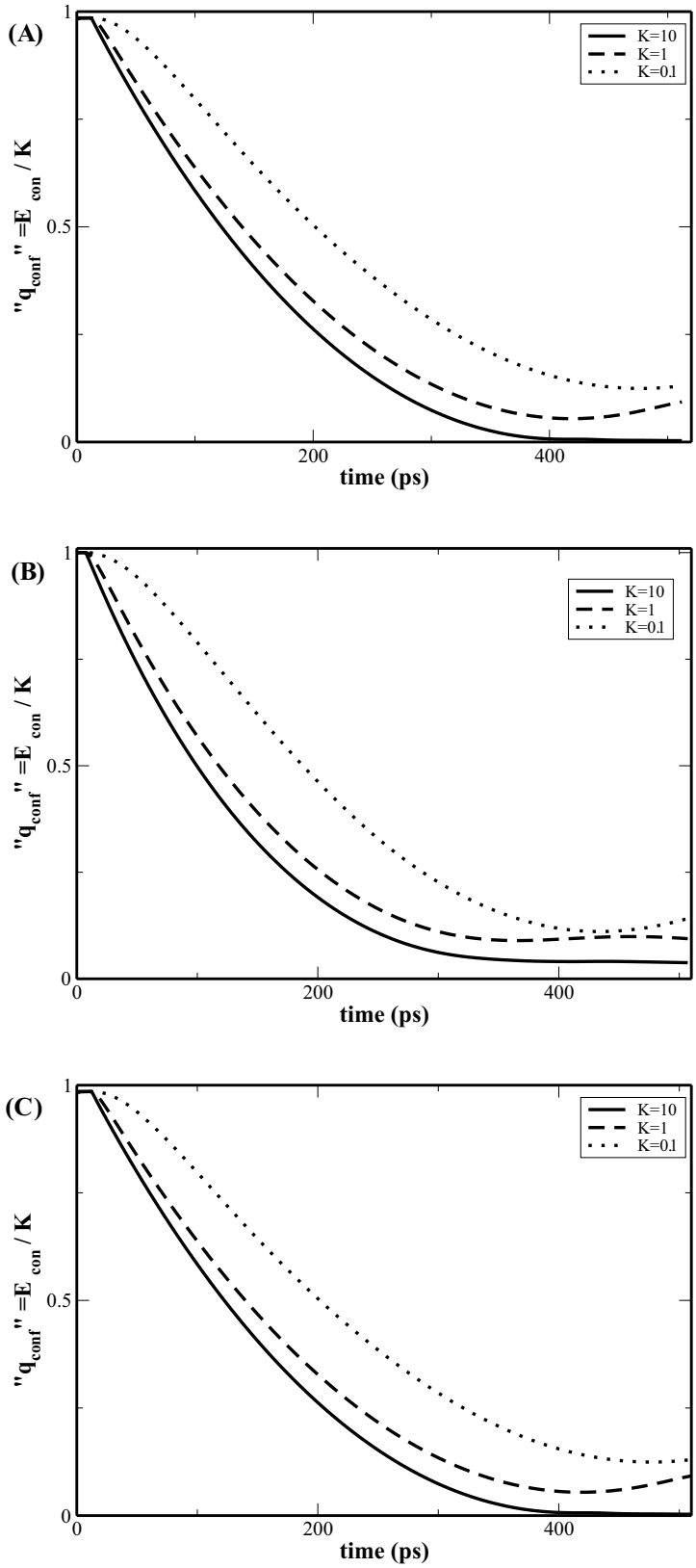

Fig. S6. The time dependence of the effective conformational coordinate for trajectories that move from the open to closed configurations with different constraints in the explicit model (*A*), the CG model with optimized friction (*B*), and the 2-D model (*C*).

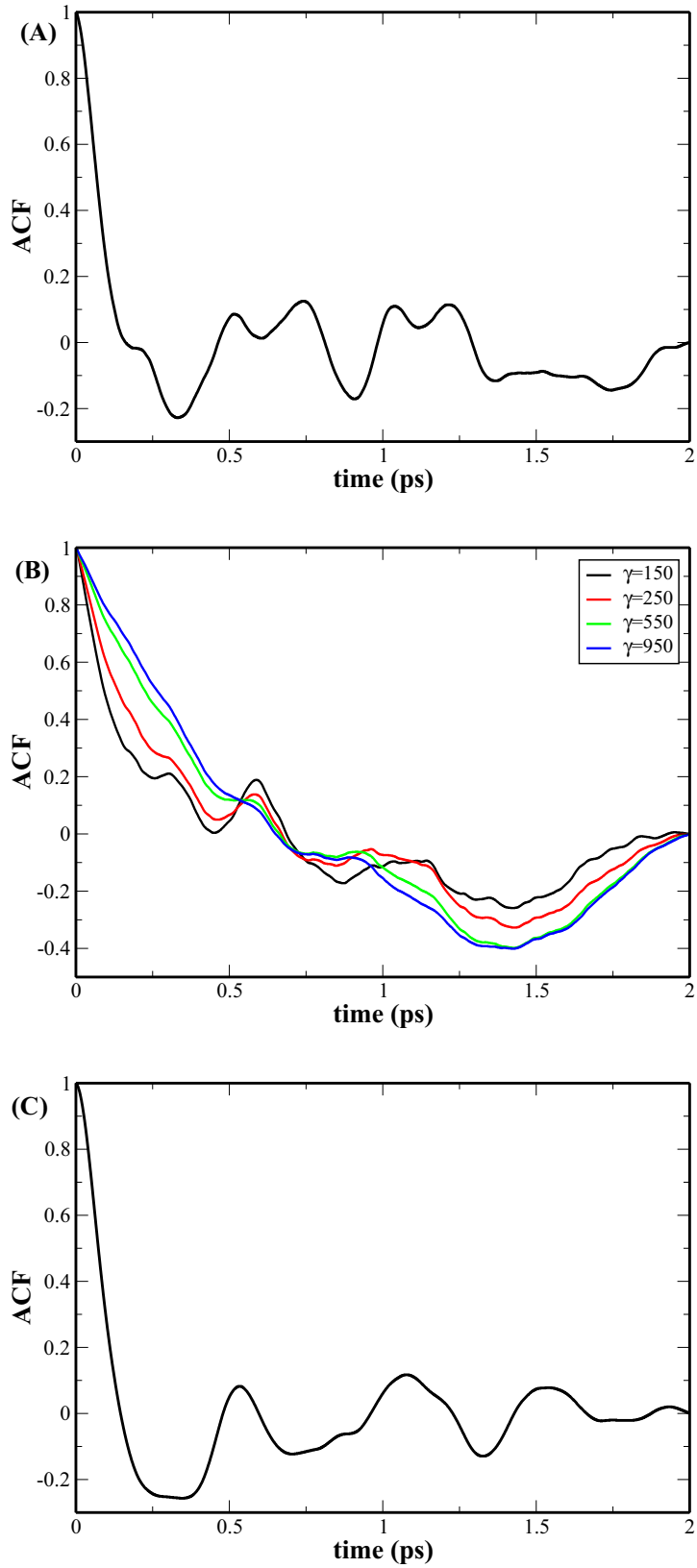

Fig. S7. The short-time ACFs of the conformational coordinate of the full (*A*), CG (*B*) and the 2-D (*C*) models. Four different values of γ_q (i.e., 150, 250, 550, and 950 ps^{-1}, respectively) were used in the CG model, whereas for the 2-D model we used a γ_{conf} of 10 ps^{-1}. The use of different values in the CG model illustrates our fitting procedure, as discussed in *Renormalizing the Landscape and Dynamics of Enzymatic Reactions.*

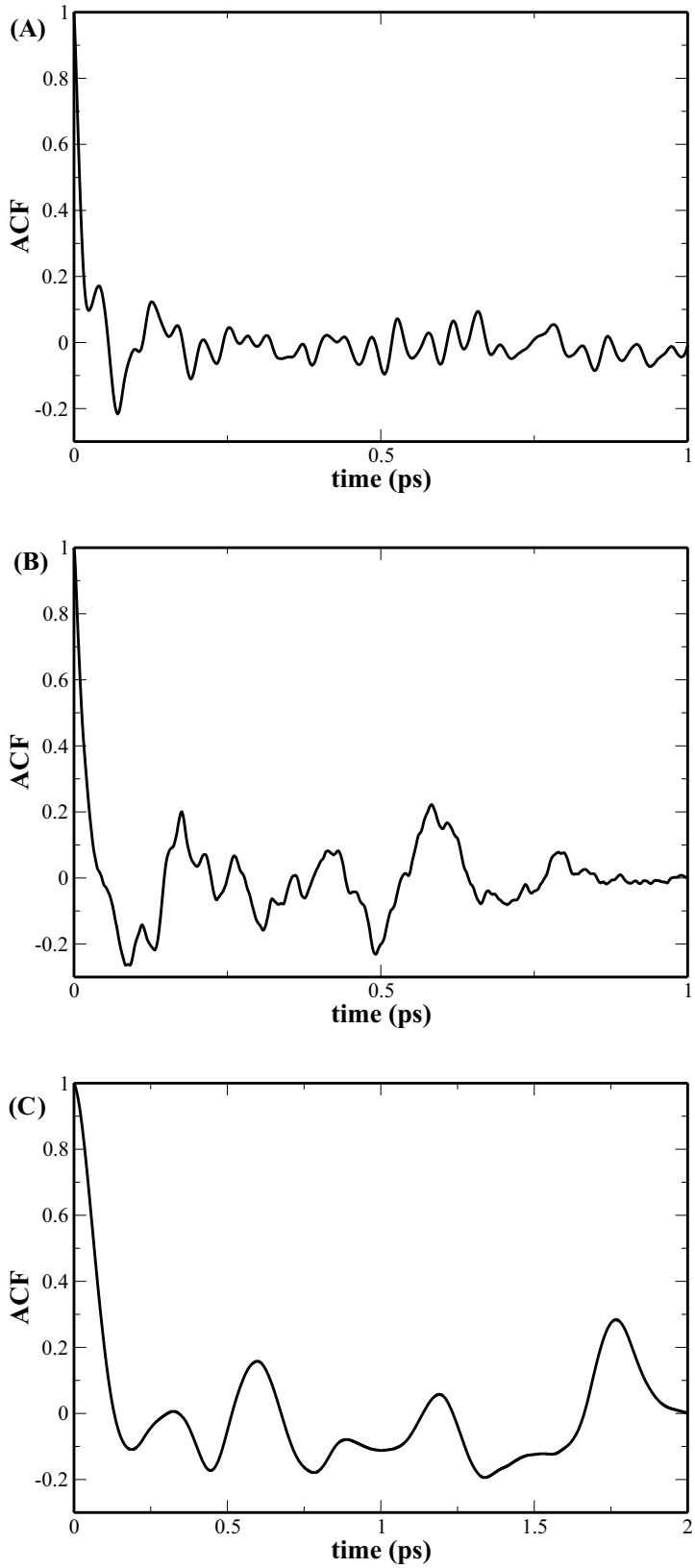

Fig. S8. The short-time dynamics of the chemical coordinate of the explicit (*A*), CG (*B*) and the 2-D (*C*) models. The optimized value of γ_q for the CG model was 250 ps^{-1}, whereas the optimal value of γ_{chem} for the 2-D model was found to be 10 ps^{-1}.

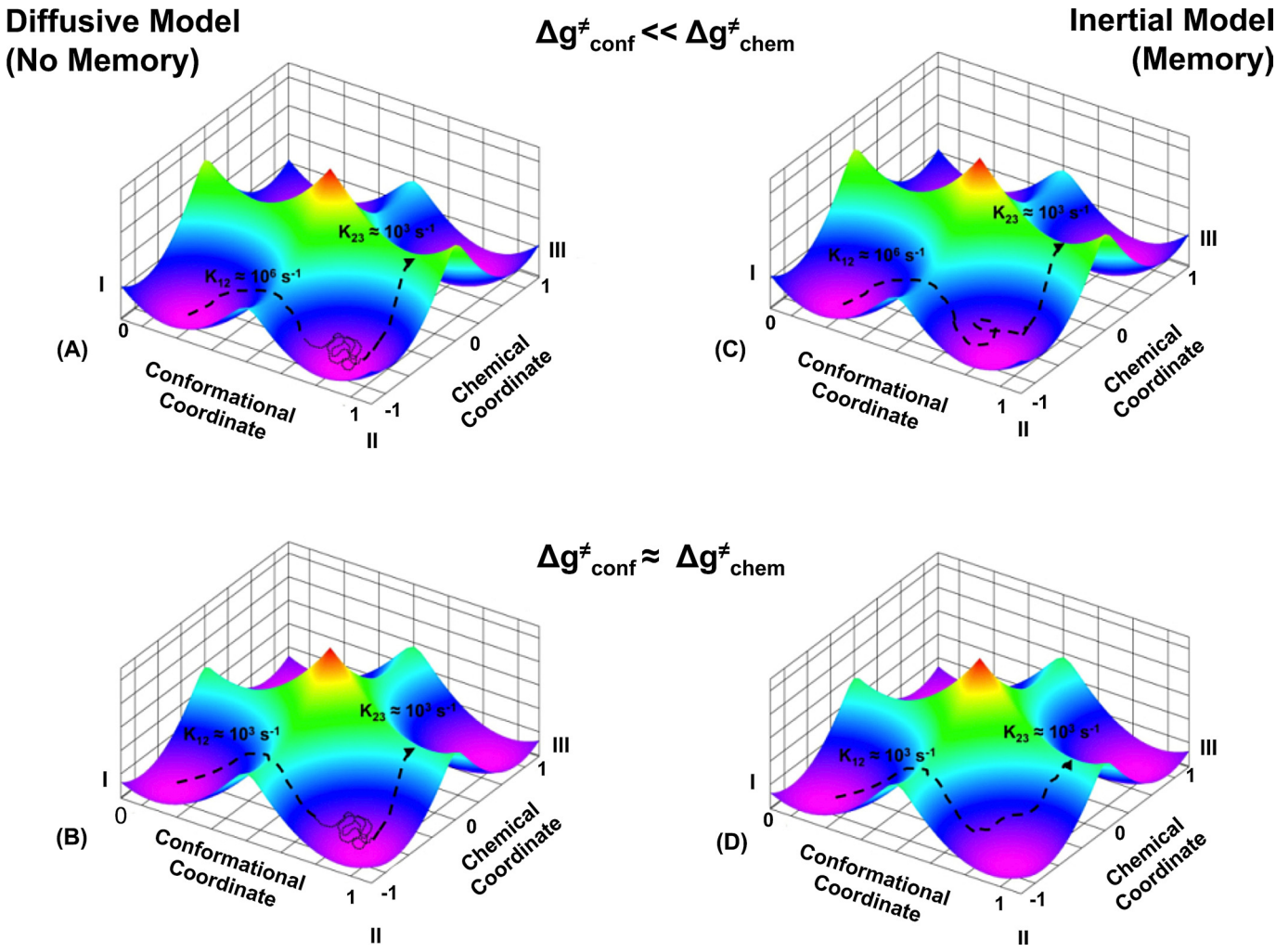

Fig. S9. A schematic depiction of the diffusive (*A* and *B*) and the inertial (*C* and *D*) models. These two limiting models are shown in the case where the conformational barrier is much smaller than the chemical one (i.e., $\Delta g^{\neq}_{conf} \ll \Delta g^{\neq}_{chem}$; *A* and *C*), and where the two barriers are similar (i.e., $\Delta g^{\neq}_{conf} \approx \Delta g^{\neq}_{chem}$; *B* and *D*).

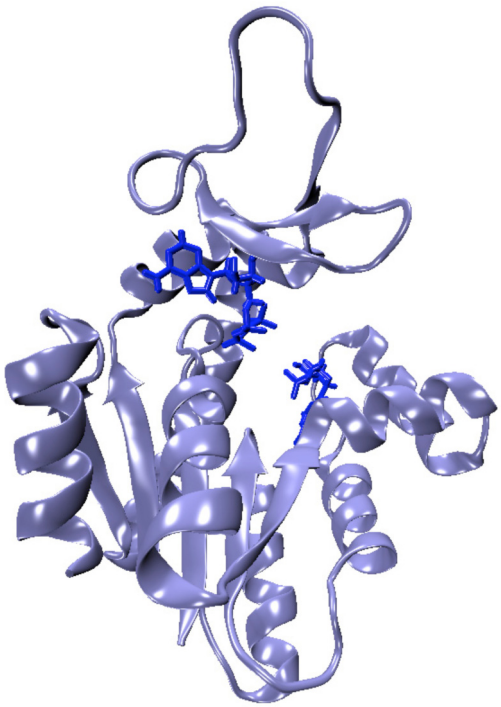

Movie S1. This movie depicts the motion obtained when forcing the long timescale conformational dynamics of the 2-D model to reproduce the experimentally observed values of k_{open} and k_{close} (where k_{close} is obtained from k_{open} by using a detailed balance), and subsequently mapping the resulting motion onto the CG model.

Movie S1 (MOV)